

NLTE Monte Carlo Radiative Transfer: I. The Thermal Properties of Keplerian Disks around Classical Be Stars

A. C. Carciofi

Instituto de Astronomia, Geofísica e Ciências Atmosféricas, Rua do Matão 1226, Cidade Universitária, 05508-900, São Paulo, SP, BRAZIL

carciofi@usp.br

and

J. E. Bjorkman

Ritter Observatory, M.S. 113, Dept. of Physics and Astronomy, University of Toledo, Toledo, OH 43606-3390

ABSTRACT

We present a 3-D NLTE Monte Carlo radiative transfer code that we use to study the temperature and ionization structure of Keplerian disks around Classical Be stars. The method we employ is largely similar to the Monte Carlo transition probability method developed by Lucy. Here we present a simplification of his method that avoids the use of the macro atom concept. Our investigations of the temperature structure of Be star disks show that the disk temperature behavior is a hybrid between the behavior of Young Stellar Object (YSO) disks and Hot Star winds. The optically thick inner parts of Be star disks have temperatures that are similar to YSO disks, while the optically thin outer parts are like stellar winds. Thus, the temperature at the disk midplane initially drops, reaching a minimum at 3–5 stellar radii, after which it rises back to the optically thin radiative equilibrium temperature at large distances. On the other hand, the optically thin upper layers of the disk are approximately isothermal — a behavior that is analogous to the hot upper layers of YSO disks. Interestingly, unlike the case of YSO disks, we find that disk flaring has little effect on the temperature structure of Be star disks. We also find that the disks are fully ionized, as expected, but there is an ionization minimum in the vicinity of the temperature minimum. The deficit of photoionization at this location makes it the most likely site for the low ionization state lines (e.g., Fe II) that produce the shell features observed in Be stars. Finally, we find that, despite the complex temperature structure, the infrared excess is well-approximated by an equivalent

isothermal disk model whose temperature is about 60% of the stellar temperature. This is largely because, at long wavelengths, the effective photosphere of the disk is located in its isothermal regions.

Subject headings: radiative transfer — stars: emission line, Be — circumstellar matter

1. Introduction

Circumstellar disks occur in a wide variety of astrophysical systems, ranging from Young Stellar Objects (YSOs) to rapidly rotating main sequence B stars (the Be stars) to highly evolved systems like cataclysmic variables, black holes, and perhaps asymptotic giant branch (ABG) stars and luminous blue variables (LBVs). In general, such disks tend to form whenever there is an accreting or outflowing circumstellar envelope in which the radial flow speed is small compared to the rotation speed. These disks reprocess the starlight, typically producing a strong infrared (IR) excess. Furthermore, these disks can be quite optically thick at some wavelengths, while being optically thin at others. Consequently, the radiation field at a given point can be quite non-local and anisotropic. In this paper, we develop a non-local thermodynamic equilibrium (NLTE) Monte Carlo radiation transfer code that may be applied to study differentially moving three-dimensional circumstellar envelopes. As a particular application of this code, we study the temperature structure of the disks around Be stars.

The circumstellar environment of Be stars has been studied extensively in the past few decades (see Porter & Rivinius 2003, for a recent review). Both observational and theoretical evidence strongly suggests that most of the circumstellar matter is contained in a very dense, geometrically thin disk (Quirrenbach et al. 1997; Wood, Bjorkman, & Bjorkman 1997). Since the stellar temperature is quite high, these disks are expected to be completely ionized and devoid of dust, so the disk opacity (primarily from hydrogen and free electrons) is much better understood than, for example, YSO disks (where the dominant opacity source is dust, whose size distribution, chemical composition, and even spatial distribution is rather uncertain). What is less well-determined is the detailed structure (density, temperature, ionization fraction, and velocity) of Be star disks.

Kinematic information about the disk can be obtained from the disk emission lines. These line profiles are often double-peaked with full widths (in the wings) that exceed the $v \sin i$ of the star by about 20% (Hanuschik 1996), so the disk must rotate faster than the star. Based on the symmetry of the hydrogen Balmer line profiles and, especially the optically thin

Fe II lines, it appears that the expansion velocity, v_r , of the disk must be much less than its rotation speed, v_ϕ (Hanuschik 1988, 1995, 1996, 2000). Studies that try to determine the rotation speed as a function of radius are less conclusive. Using a power-law parameterization, $v_\phi \propto r^{-j}$, Hummel & Vrancken (2000) find that they cannot distinguish between angular momentum-conserving ($j = 1$) and Keplerian ($j = 1/2$) velocities for optically thin lines, but for optically thick lines they find $v_\phi \propto r^{-0.65}$, favoring Keplerian orbital motion. Theoretical evidence for Keplerian rotation is provided by the observation of periodic variations in the shape of the double-peaked emission line profiles. During these variations, the amplitudes of the violet and red emission peaks change in an antisymmetric fashion (so-called V/R variations). Such behavior can be explained theoretically by a precessing one-armed density wave (Okazaki 1991), but on theoretical grounds such density waves require a Keplerian velocity structure (Okazaki 1991). We conclude, therefore, that the disk has a Keplerian orbital velocity with $v_r \ll v_\phi$.

The IR excess of Be stars arises from free-free (f-f) emission in the disk (Gehrz, Hackwell, & Jones 1974). Since the f-f opacity increases with wavelength, the slope of the IR excess can be used to probe the radial density structure of the circumstellar envelope (Wright & Barlow 1975; Lamers & Waters 1984). Assuming an isothermal disk with a radial power law for the density, $\rho \propto r^{-n}$, this technique gives density exponents in the range $n = 2\text{--}3.5$ (Waters 1986; Coté & Waters 1987; Waters, Coté, & Lamers 1987). It should be noted however, that this result depends on the radial structure of the disk temperature (see Cassinelli & Harmann 1977, which shows how the slope of the IR excess depends on the temperature gradient).

Although quite sophisticated radiative equilibrium models have been developed that can determine the 2-D temperature structure of YSO disks and envelopes (e.g., D’Alessio et al. 1998; Wood et al. 2002; Dullemond 2002; Whitney et al. 2003; Walker et al. 2004), we are only now beginning to understand the temperature structure of Be star disks. Models of spherically expanding stellar winds suggested that, as a consequence of the Cayrel effect (Cayrel 1963), the wind ionization fractions would “freeze” (i.e., be constant) at large radii and that the temperature would become isothermal with a temperature of about $0.8T_{\text{eff}}$ (Klein & Castor 1978, however later work by Drew 1989, who included cooling by heavy elements, shows the temperature is not particularly isothermal, slowly falling to less than 60% T_{eff} at large distances). In any case, the usual assumption for the disk temperature was to hope for a similar situation and to assume that the disk was isothermal with a temperature $T_d = 0.8T_{\text{eff}}$ (e.g., Waters 1986). The first attempts to calculate the disk temperatures were performed by Millar & Marlborough (1998), who implemented the radiative equilibrium condition within the Poekert & Marlborough (1978) code. Note however, that the Poekert & Marlborough code does not perform a full two-dimensional solution to the radiative

transfer problem; it instead employs several approximations to estimate the hydrogen level populations. In subsequent papers, Millar & Marlborough (1999a) approximated the effects of diffuse emission by employing the “on-the-spot approximation”, while Jones, Sigut, & Marlborough (2004) included cooling by Fe line emission. In general, they find that the disk temperature in the mid-plane is quite low, while the upper layers of the disk are hot. This fundamental work shows that the disk is certainly not isothermal, bringing into question the Waters et al. density results. For this reason, Millar & Marlborough (1999b) calculated the temperature for the Waters (1986) density model. They concluded that the average disk temperature is a factor of 2–3 lower than that assumed by Waters. An additional effect (not addressed by Millar & Marlborough 1999b) is that the non-isothermal temperature structure may alter the slope of the IR continuum, thereby changing the estimates of the radial density exponent, n .

In this paper, we build upon and extend the results of Millar & Marlborough (1998, 1999a,b) to study more fully the temperature and ionization structure of the disk. In particular, we investigate what physically determines the temperature behavior of the disk, and we compare this behavior to that of YSO accretion disks and stellar winds. We also examine the effects of a non-isothermal disk temperature on the IR spectral energy distribution (SED) of Be stars. To do so, we have developed a Monte Carlo radiative transfer code (presented in section 2) that fully solves the 3-D NLTE problem and radiative equilibrium temperature. In section 3, we present test calculations used to verify both the method and the computer code. The disk model used in this paper is described in Section 4. In Section 5, we investigate the dependence of the temperature, hydrogen level populations, and ionization fractions on model parameters such as the disk density and geometry. Similarly, we investigate how the temperature structure alters the slope of the IR excess. Finally, we summarize our results in Section 6.

2. The Monte Carlo Code

One of the greatest assets of the Monte Carlo (MC) method is its flexibility and ease of implementation, especially as the complexity of the system increases. Although traditional radiative transfer methods are much more computationally efficient for simple configurations (e.g. plane-parallel or spherical geometries), for more complex situations (e.g., 3-D geometries, anisotropic scattering, and complex frequency redistribution processes) the MC method is frequently the only viable alternative. Furthermore, the relative efficiency of Monte Carlo methods increases as the number of spatial dimensions, frequencies, and anisotropy of the radiation field increases.

Recently, Lucy (2002, 2003, 2005, hereafter L02, L03, and L05) developed a Monte Carlo transition probability method to solve the statistical equilibrium problem. His method employs indivisible energy packets to describe the exchange of energy between photons, *macro atoms* (an ensemble representation of the atomic excitation throughout a finite volume element), and free electrons. The energy packets contain either radiative energy (*r*- packets) or kinetic energy (*k*-packets). When an energy packet (either radiative or kinetic) is absorbed by a macro atom, the macro atom randomly performs internal transitions (using an effective transition probability array) between its energy states until it emits a new energy packet (either kinetic or radiative); see Figure 1. Since any photon absorption is eventually followed by emission of an equal energy photon packet, this method automatically enforces radiative equilibrium (in the rest frame of the gas). The key ingredient of this method is the effective transition probability array, and L02 shows how to choose these probabilities so that the internal transitions of the macro atoms will reproduce the statistical equilibrium equations. Since the transition probabilities (effectively they are the net rates between levels) depend on both the values of the mean intensity in each line and the level populations, their solution requires iteration.

L02 shows that this technique correctly reproduces the line and continuum emissivities, the “ Λ -iteration” converges, and on average there are only about two internal transitions per photon-macro atom interaction. In subsequent papers (L03 and L05), Lucy applied this method to the non-trivial problem of calculating the hydrogen level populations and electron temperature in the expanding shell of a type II supernova. He also studied the convergence behavior and demonstrated that the correct solution can be achieved with a reasonable amount of computing time.

In 2002-2004, we independently developed a method for solving both the statistical and radiative equilibrium in circumstellar winds and disks of hot stars. Our method is largely similar to the one described in L03, in that we measure the rates (radiative, heating, and cooling) using essentially identical methods — path length sampling, (see Lucy 1999, hereafter L99), so rather than reproducing those formulae here, we simply refer the reader to sections 5 and 6 of L03 and section 2 of L05. However our method differs from Lucy’s in one key area: the photon-atom interactions. In the following, we present a short description of our method, focusing on the differences with Lucy’s method.

The essence of any method for solving the radiative transfer problem is to correctly describe the radiation field everywhere in the so-called interaction region (the physical medium wherein the radiation propagates). In the MC method, this is accomplished statistically by simulating the random propagation of N photon packets (PPs) through the medium, where they are scattered, absorbed, and reemitted until they eventually leave the interaction re-

gion. A convenient choice is to emit equal-energy monochromatic PPs from the star (as a consequence, packets of differing frequencies contain different numbers of physical photons). The condition of radiative equilibrium then implies that whenever a PP is absorbed, it must be reemitted at the same location with the same energy (in the rest frame of the fluid; in the stellar frame, the packet energy changes, owing to the doppler shift between the different reference frames). This device automatically ensures flux conservation; i.e., the flux is everywhere divergence free (Lucy 1999; Bjorkman & Wood 2001). Although the (rest frame) packet energy does not change, the new direction and frequency of the PP must be chosen to reproduce the emissivity j_ν of the medium at that location.

To solve the statistical equilibrium rate equations, the following procedure is employed. Initially, the interaction region is divided into a number of cells. In each cell, the gas state variables (density, velocity gradient, kinetic temperature, and level populations) are assumed to be constant. The simulation starts with an initial estimate of the state variables for each cell. While the simulation is performed, the radiative rates, as well as the heating rate, of the gas are sampled as photons pass through each cell. At the end of the MC simulation, the accumulated radiative and heating rates are used to update the cell level populations and kinetic temperature. A new simulation then is performed using the updated values of the state variables. This procedure is repeated until the state variables converge to their equilibrium values for all cells.

From the above description, it is evident that two key points are necessary for the method to succeed. First, there must be an efficient way to sample all the radiative transitions and heating rates. An elegant and efficient solution for this was proposed by L99 and further developed in L03. In section 2.1.2, we describe how to more efficiently sample the bound-bound (b-b) rates. The second critical point is that the MC simulated radiation field has to statistically reproduce the “true” radiation field of the system. Because every PP absorption is immediately followed by *in situ* reemission, this condition reduces to sampling correctly the frequency and direction of the reemitted PPs.

Lucy’s method (fig. 1) simulates the interaction of the radiation with matter by tracking transitions of his macro-atoms. When a PP (*r*-packet) undergoes an absorption event (determined by the opacities), it will either activate a macro atom (for instance, through b-b or bound-free transitions) or be converted into a *k*-packet (for example, via f-f absorption). A series of internal transitions (controlled by the MC transition probabilities, L02) eventually leads to the conversion of the energy back into an *r*-packet. Thus, Lucy’s method is a scheme for sampling the frequency of the reemitted PPs.

The approach we adopt in this paper differs from Lucy’s in that we do not use his MC transition probabilities to sample the frequency of the reemitted PP. Instead, we bypass

his macro-atoms and directly sample the frequency from the total emissivity of all possible emission processes. Thus our emission process is completely unlinked from the absorption process. For example, a photon may be absorbed by a b-b transition and then reemitted by a f-f process. This may seem peculiar, but all that matters is that at the end of the simulation, we produce the correct total luminosity and frequency distribution for each process.

For a given cell j , the total luminosity of a given process k is

$$L_j^k = \int_{V_j} dV \int_0^\infty 4\pi j_\nu^k d\nu. \quad (1)$$

where j_ν^k is the emissivity of process k and the first integral is performed over the cell volume V_j . When a PP is absorbed in cell j , we select the physical process k that reemits the PP, determined by the minimum value of k satisfying

$$\xi < \sum_{i=1}^k L_j^i / L_j, \quad (2)$$

where ξ is a uniform random number in the interval $(0, 1)$, and the total luminosity of the cell

$$L_j \equiv \sum_i L_j^i. \quad (3)$$

Once the physical process is chosen, the frequency of the emitted PP is sampled using standard MC techniques (see section 4 of L03).

From the point of view of computer coding, our method has the advantage of being easier to implement (but one should note that the implementation of macro-atoms does not require a particularly large coding effort). Since we dispense with the macro-atom device, we do not need to track their internal transitions, which in principle increases the relative speed of our code (but, this may not be a large effect since there were only two internal transitions per interaction for the case studied by L02). Similarly, there is no need to convert energy packets back and forth between r -packets and k -packets. On the other hand, it is not clear which method will converge faster. Both methods use the previous line intensities to calculate their reemission probabilities, and the two methods are rigorously equivalent for a system already in equilibrium. However, out of equilibrium, the two methods differ. Our emissivities are constant during a given iteration, but Lucy's method uses conditional transition probabilities, which may somewhat adapt the emissivities to the new values of the line intensities. We suspect, therefore, that Lucy's method might have a somewhat better convergence rate.

Finally, we point out that even using the efficient intensity estimators of L03 and L05, the computational demand for 2-D and 3-D problems is enormous, requiring a parallel-computing

cluster to make the run times practical. Fortunately, the structure of the algorithm is well-suited for parallel computation. The problem is “embarrassingly parallel” — one simply divides the total number of photon packets into batches that run independently on each processor. For the 2-D models shown in Sections 5, we used a 96-node Beowulf cluster (with 1.7 GHz Athlon CPUs). One iteration for the level populations and kinetic temperature requires about 15 minutes on this cluster (using $N = 3 \times 10^7$ PPs). Since the number of iterations required is about 10–15, one model takes a few hours to complete.

2.1. Simulations for a Small Frequency Range

A common problem for full-spectrum MC codes is that the radiation field is typically under-sampled at frequencies where the mean intensity is low. This happens because the number of PPs per frequency interval is proportional to the mean intensity. As a result, calculating the emergent flux at those frequencies requires a very large number of PPs for the simulation. Similarly, calculating the emergent flux for a very narrow frequency range (as is the case for line profiles) can be problematic because the number of PPs in that range is small.

A related issue is determining the b-b rates required to solve the statistical equilibrium equations, because sampling each transition requires a large number of PPs in a small frequency range. For instance, suppose that the mean intensity at a given point of the interaction region is given by a Planck function. The ratio of resonant H α PPs to the total number of PPs is approximately

$$\frac{N_{\text{H}\alpha}}{N} \approx \frac{(v_{\text{max}}/c) \nu_{\text{H}\alpha} B_{\nu}(\nu_{\text{H}\alpha}, T)}{\sigma T^4}, \quad (4)$$

where v_{max} is the maximum macroscopic velocity of the gas and σ is the Stephan-Boltzmann constant. For $v_{\text{max}} = 1000 \text{ km s}^{-1}$ and $T = 16000 \text{ K}$, this ratio is about 10^{-4} , which illustrates the low number of PPs available for sampling the b-b rates. If one considers that the main source of exciting PPs comes from the external radiation source (the star), and that those PPs would be split over the very large number of cells necessary for 2-D or 3-D problems, it is easy to see that a huge number of PPs would be necessary to correctly sample the b-b rates. The solution to this problem is simple: limit the frequency range of the MC simulation to the vicinity of the line of interest, and sample each b-b transition separately.

Consider a star surrounded by an envelope that is divided into M cells. The total energy emitted by the star per unit time in the frequency range ν_0 and ν_1 is

$$L_{\star} = 4\pi R_{\star}^2 \int_{\nu_0}^{\nu_1} \mathcal{F}_{\nu}^{+} d\nu, \quad (5)$$

where \mathcal{F}_ν^+ is the outward flux at the stellar surface. Similarly, the luminosity of process k in cell j , L_j^k , can be calculated from eq. (1), using the appropriate frequency range in the integral. The total energy emitted by the cell, L_j , is calculated from eq. (3), and the total energy emitted by the envelope is given by

$$L_{\text{env}} = \sum_{j=1}^M L_j. \quad (6)$$

Given the energies calculated above, the MC calculation proceeds step-by-step as follows:

1. A new PP is generated. If $\xi < L_\star / (L_\star + L_{\text{env}})$ the PP is emitted by the star (go to step 2), and if $\xi > L_\star / (L_\star + L_{\text{env}})$ the PP is emitted by the envelope (go to step 3).
2. The position on the stellar surface is sampled randomly, the PP frequency is chosen from the stellar flux, \mathcal{F}_ν^+ , over the relevant frequency range, and the propagation direction is sampled from the limb darkening law. Proceed to step 6.
3. The cell j that emits the PP is sampled using the relation $\xi < \sum_{i=1}^j L_i / L_{\text{env}}$.
4. The process k that emits the PP in cell j is sampled using eq. (2).
5. The position of the PP inside the cell is chosen randomly, and the PP propagation direction is chosen accordingly to the process of emission. For example, the direction distribution for line emission is given by the Sobolev escape probability.
6. The PP is propagated through the medium using standard MC techniques until it leaves the envelope. If the PP is absorbed or hits the star, it is destroyed. Return to step 1 until all N PPs are generated.

2.1.1. Detailed Spectra

The above procedure can be used for the calculation of emergent spectra, both where the flux is low (e.g., the IR flux in hot stars) and when the frequency range is small (e.g., a detailed calculation of the shape the balmer jump). Recall that in the radiative equilibrium scheme, a PP may be absorbed and reemitted many times before escaping — a time-consuming process — while in the above procedure the PP is simply destroyed. Thus in addition to enabling the calculation of multi-frequency radiative transfer in arbitrary frequency ranges, the above procedure also has the advantage of performing much quicker spectral syntheses. Furthermore, it automatically includes anisotropic scattering and polarization effects that are difficult to include in traditional post-processing routines.

2.1.2. Sampling Bound-Bound Rates

Finally, we use the above technique to sample the b-b rates in the following way. We first run a standard radiative equilibrium simulation to calculate all the radiative and heating rates, apart from the b-b rates. Then a series of simulations are performed to sample individually the rates for each b-b transition. By choosing a frequency range $[\nu_L(1 - 2v_{\max}/c), \nu_L(1 + 2v_{\max}/c)]$, where ν_L is the frequency of the transition (i.e., centered on the line of interest), we ensure that we properly account for the coupling to all possible processes, including other emission lines.

3. Numerical Tests

Here we verify our code results and test the convergence of our algorithm. We present two test cases: 1) a blackbody cavity, which has a simple analytic solution, and 2) the non-trivial problem of a spherically symmetric expanding stellar wind.

3.1. Blackbody Cavity

This test consists of a spherical cavity whose boundary emits a blackbody spectrum of a given temperature. The cavity is filled with hydrogen with constant density throughout. Each PP emitted by the cavity wall undergoes a random series of scatterings and absorptions followed by *in situ* reemissions as described in section 2, but eventually the PP is absorbed (and destroyed) by the blackbody cavity wall, whereupon another PP is emitted until the total number PPs have been run.

A blackbody cavity is an especially convenient test because the gas should come to complete thermodynamic equilibrium with the wall. Thus the state variables of the gas depend solely on the temperature of the cavity’s wall, T_{cav} , and the level populations and ionization fraction should be given by the Boltzmann-Saha distribution. Furthermore, the local radiation field should be a Planck function, and all radiative rates should attain their LTE values. Finally, the kinetic temperature of the electrons should also be T_{cav} .

We used this setup to test several aspects of our method. A trivial but important situation is to set the initial level populations and electron temperature to their correct equilibrium values; i.e., $T_e = T_{\text{cav}}$ and $n_i = n_i^*$, where the asterisk indicates LTE level populations. In this case, one expects that, if the rates are being properly sampled, the state variables should oscillate around the LTE values as a result of MC statistical sampling

errors. Furthermore, the magnitude of the oscillation should decrease approximately¹ as $1/\sqrt{N}$. This test is also important because it demonstrates the stability of a converged solution. The results for 30 iterations with initial conditions $T_{\text{cav}} = 20000$ K and hydrogen number density $n_H = 10^{14}$ cm⁻³ are shown in Figure 2. The simulation in the left panel employed $N = 10^4$ PPs, while the right panel had $N = 10^7$. As expected, the results for T_e and n_i oscillate around the correct equilibrium values, and the magnitude of the oscillation decreases as N increases. The R.M.S. relative error

$$\epsilon_S = \left[\frac{1}{n_{\text{it}} - 1} \sum_{i=1}^{n_{\text{it}}} (S_i - S^*)^2 / (S^*)^2 \right]^{1/2}, \quad (7)$$

where S is the state variable of interest, is indicated for hydrogen levels 1 and 10, as well as the electron temperature. Note that the R.M.S. errors decrease roughly by the expected amount ($\sqrt{10^3}$).

In the next series of tests, we varied the initial values of the state variables to verify that the results did converge to their correct values. As an example, Figure 3 shows 30 iterations of the ground level population for three values of N (10^3 , 10^4 , and 10^7). The population was increased initially by a factor of 10^3 , and it converges to the correct value (shown as a straight line in the figure) after about 10 iterations. More importantly, the level population converges even in the presence of the very large sampling errors for the $N = 10^3$ case.

The high precision we were able to obtain for the level populations and electron temperature in the blackbody cavity test verifies the validity and the correctness of our implementation of the method described in the last section. In addition, it shows that, as already demonstrated by L02, the random errors intrinsic to the Monte Carlo method do not prevent the convergence of the state variables. It is important to emphasize this last remark because, when the method is applied to 2-D or 3-D geometries, one may easily run into situations for which given parts of the simulation may be under-sampled. An example of such a situation is the equatorial region of optically thick disks, which is shielded from the stellar ionizing radiation by the disk’s upper layers.

Finally, we would like to comment that the blackbody cavity test has proven extremely useful during the development phase of the code. In particular, detailed balance occurs in LTE, so one can turn on and off individual processes (e.g., f-f emission and absorption), and the results should not change. This permits one to test separately each part of the implementation. Similarly, sampling the local radiation field and looking for departures

¹Since there is a nonlinear relationship between the rates and the state variables, the statistical error will not follow exactly a Poisson distribution (unless the fluctuations are small).

from a Planck function is especially useful for diagnosing errors.

3.2. NLTE Test

To assess the NLTE results for our method and to verify the Sobolev escape probabilities for the spectral lines (which modify the rate equations), we applied our code to the 1-D problem of a spherical expanding wind around a hot star, and compared our results to those given by the well-established code of MacFarlane et al. (1993). We were able to match MacFarlane’s results for a wide range of stellar temperatures, wind density, and velocity. An example comparison is given by Figure 4, which shows the $n = 2$ hydrogen level populations for a B2 V star ($T_{\text{eff}} = 20000\text{K}$, $R_{\star} = 6.6R_{\odot}$), surrounded by a stellar wind with a β -law velocity

$$v_r = v_{\infty} \left(1 - \frac{R_{\star}}{r}\right)^{\beta}, \quad (8)$$

with $v_{\infty} = 1600 \text{ km s}^{-1}$ and $\beta = 0.8$. For all mass-loss rates shown ($\log \dot{M} = -8.7, -7.7$ and -6.7), the difference between the results is typically less than 0.1%.

4. Disk Model

As discussed in the introduction, observational evidence indicates that the circumstellar disks of Be stars are geometrically thin, optically thick disks, whose outflow velocities are small in comparison to their rotation speeds. Dynamically this requires that the disk be pressure supported in the vertical direction and centrifugally supported in the radial direction. For this reason the disk structure is most likely to be that of a Keplerian hydrostatically supported disk. How material is injected at Keplerian speed into this disk is still unclear, but after it is injected, the gas will spread outward (and inward if it is injected at intermediate radii), owing to viscous effects (Lynden-Bell & Pringle 1974).

Determining the self-consistent structure for a Keplerian disk is a somewhat complicated problem, because the disk temperature controls its geometry (via the hydrostatic equilibrium equation), which in turn determines the heating and hence temperature of the disk (see Kenyon & Hartmann 1987). Rather than solving the hydrostatic equilibrium equation (which we plan to investigate in a subsequent paper), we instead assume that the disk geometry is a known function. For our present purposes — an initial investigation of the temperature and ionization structure of the disk — we feel this is a reasonable approach.

Studies of pre-main-sequence accretion disks (see Hartmann 1998, for a review) show

that the disk pressure scale height $H = (a/v_\phi)\varpi$ is small (since the orbital speed, v_ϕ , is typically much greater than the isothermal sound speed a), so the disk is geometrically thin, and the disk temperature typically falls (roughly) as a power-law with radius. Assuming the disk is vertically isothermal, the disk density structure is given, in cylindrical coordinates (ϖ, z, ϕ) , by

$$\rho(\varpi, z) = \rho_0 \left(\frac{R_\star}{\varpi} \right)^n \exp \left(-\frac{z^2}{2H^2} \right) \quad (9)$$

(see, for example, Bjorkman 1997). For steady-state isothermal outflow, the radial density exponent $n = 3.5$ (Lee et al. 1991; Porter 1999). The vertical structure is the familiar Gaussian result for pressure-supported disks with a scaleheight

$$H(\varpi) = H_0 \left(\frac{\varpi}{R_\star} \right)^\beta, \quad (10)$$

where

$$H_0 = \frac{a}{v_{\text{crit}}} R_\star, \quad (11)$$

and $v_{\text{crit}} = \sqrt{GM/R_\star}$ is the critical velocity of the star. The disk flaring exponent β depends on how the disk temperature falls with radius. For optically thick, infinitesimally thin reprocessing disks, $T \propto \varpi^{-3/4}$, which gives $\beta = 9/8$ (Kenyon & Hartmann 1987, but see D’Alessio et al. 1998), while for optically thin stellar winds, the temperature is roughly isothermal (Klein & Castor 1978), so $\beta = 1.5$.

The disk flaring parameter β controls the shape of the disk surface and hence its heating versus radius. As such, it is the primary parameter, along with density, that controls the temperature and ionization structure of the disk. Consequently for this paper, we adopt the above structure for the circumstellar disk, and let β and ρ_0 be free parameters. Some models of Be star disks assume the disk is truncated at some point, perhaps by a binary companion, so we also assume the disk has a finite outer radius R_d , which we set to $1000R_\star$.

To complete our disk model, we have to specify the hydrogen model. We adopt a 25-level model of the H atom, where the first 12 levels are explicit NLTE levels, and the remaining 13 upper levels are implicit levels with LTE populations (with respect to the continuum). Each level has a consolidated statistical weight $g_n = 2n^2$.

For the description of the central star we have to specify its effective temperature and surface gravity, which defines the Kurucz model atmosphere (Kurucz 1979, 1994) that we use as our input spectrum. We have to specify, in addition, the stellar radius and mass, which determine the critical velocity and scaleheight H_0 . Previously, we modeled the disk of ζ Tauri, B3IV (Wood et al. 1997), so we arbitrarily chose this spectral type for our stellar parameters (see Table 1).

4.1. Grid Definition

As described in section 2, the MC calculation is performed for a discretized model of the disk with each of the model unknowns (rates, temperature, level populations) being constant throughout a given cell. Thus, it is essential that the grid be constructed to minimize (as far as practical) the variation of these unknowns within the cell.

The disk is divided into n_r radial shells, each of which are divided into n_μ cells in latitude and, if needed, into n_ϕ cells in azimuth. We found a total of 40 cells in radius and 40 cells in μ to be a good compromise between usage of computer memory, speed of the code, and accuracy of the result. The radial spacing is defined so that each cell has the same radial electron optical depth. This approach has the drawback that the last cell becomes very large, so we further subdivide the last cell to properly sample the outer parts of the disk. The μ -spacing is defined in such a way that each cell represents an equal linear step in density, and, consequently, the cells are smaller close to the midplane and become larger for larger z . Also, the cells become larger with increasing radius because of the disk flaring. The disk is truncated in the z -direction when the density becomes 10^{-7} smaller than the value at the midplane.

5. Results

In this section we explore the effects of the disk free parameters (ρ_0 and β) on the electron temperature and hydrogen level populations. We also investigate the effects of the temperature distribution on the IR excess. The parameters for all the models shown in the subsequent sections are listed in Table 2.

5.1. Ionization and Level Populations

The $n = 1$ and 2 level populations of hydrogen for models 01 and 04 (the density extremes) are shown in Figure 5, as a function of radius. Each panel shows the level populations at different latitudes as indicated (0° corresponds to the disk midplane). The approximations used in Millar & Marlborough (1998, 1999a) make it difficult to perform a direct comparison between our results and theirs; however, they are qualitatively similar.

In general, the disk is almost completely ionized, with the exception of the midplane. However, in none of the models does the midplane become completely neutral. For model 04 (the highest density disk), the neutral hydrogen fraction at the midplane has two maxima,

one at $\varpi \approx 6R_\star$ for which $n_1 = 20\%$ and the second at $\varpi \approx 50R_\star$ where $n_1 = 44\%$. For model 01 (the lowest density model), the two maxima are also present, but closer to the star ($n_1 = 1\%$ at $\varpi \approx 3R_\star$ and $n_1 = 6\%$ at $\varpi \approx 40R_\star$). These minima in the hydrogen ionization fraction indicate the location where the photoionizing mean intensity is smallest. The first minimum is also near the temperature minimum of the disk (see section 5.2), so this position is likely to be the location of the low ionization state lines (like Fe II) that form the shell features in Be spectra.

Another interesting feature of Figure 5 is the crossing of the low latitude $n = 1$ curves. At small radii, the lower density model (01) becomes more neutral than the higher density model (04). This apparent incongruity is a result of the higher density model being much hotter near the star than the lower density model.

5.2. Temperature

The temperature structure of model 02 is shown in Figure 6. The leftmost panel is the temperature in the vicinity of the star ($1 < \varpi/R_\star < 4$), the center panel is the temperature for intermediate distances ($1 < \varpi/R_\star < 10$), and the rightmost panel is for large distances (ϖ up to $100R_\star$). In this figure, which generally is representative of all models, we observe two regions with very distinct temperature behaviors: the midplane region (between the dashed curves, defined by $|z| \leq H$), and the upper/lower layers of the disk ($|z| > H$). In the upper layers, the temperature is nearly constant, averaging 10100 ± 1300 K (about 50% of T_{eff}). This region is optically thin for shorter wavelengths (typically $\lambda \lesssim 10 \mu\text{m}$), so it contributes very little to the disk emission at these wavelengths; however, it becomes optically thick for longer wavelengths. Thus, this layer controls the long wavelength IR excess.

For the midplane region, the temperature structure is much more complex. Beginning at the base of the disk, the temperature is high (≈ 15000 K), quickly drops to a minimum temperature of ≈ 7000 K at $\varpi \approx 4R_\star$, and rises back, reaching ≈ 11000 K at $\varpi \approx 10R_\star$, beyond which it becomes roughly isothermal. Other models show similar behavior, but the depth and location of the temperature minimum depends on the disk density (or equivalently, optical depth). Figure 7 shows the mid-plane temperature as a function of increasing density (models 01–04). Note that as the density increases, the temperature minimum becomes deeper and occurs at larger radii.

Since the disk is *strongly non-isothermal* (unlike a stellar wind), it is important to understand what determines its temperature structure. In accretion disks around young stellar objects (YSOs), the temperature typically falls as a power law with radius, $T \propto r^{-m}$,

with an exponent m in the range $1/2$ – $3/4$, depending on the disk flaring. This is because the surface of a very optically thick disk acts very much like a blackbody that reprocesses the incident starlight. Since the star illuminates the surface at an increasingly oblique angle with radius, the temperature falls faster than the usual $r^{-1/2}$ geometrical dilution of the star. For an infinitesimally thin, flat (i.e., not flared) blackbody disk, the temperature falls as $r^{-3/4}$, but close to the star a detailed integration gives

$$T_d(\varpi) = \frac{T_\star}{\pi^{1/4}} \left[\sin^{-1} \left(\frac{R_\star}{\varpi} \right) - \frac{R_\star}{\varpi} \sqrt{1 - \frac{R_\star^2}{\varpi^2}} \right]^{1/4}, \quad (12)$$

where T_\star is the temperature of the radiation that illuminates the disk (Adams, Lada, & Shu 1987, hereafter, ALS).

Using this function, we fit the mid-plane temperatures (close to the star) for each model. The resulting curves for models 01–04 are shown in Figure 7 (thick lines), while the values of T_\star along with ϖ_{dep} (the outer radius of the fitting interval) are listed in Table 2. We see that eq. (12) reproduces the initial temperature decrease quite well. However, T_\star is *larger than* T_{eff} for all models (except the lowest density model 01), and the larger the density, the larger the corresponding T_\star . It is evident, therefore, that this behavior is due to back-warming of the star (photons that hit the star are reemitted locally to simulate this effect). This result reveals a small inconsistency in our model: the back-warming is sufficiently large that the stellar photospheric temperature should be increased near the equator. We did not attempt to fully model this effect; we only reemitted the photons without raising the temperature.

Another interesting feature of Figure 7 is that, as the density increases, the departure point, ϖ_{dep} (the location where the MC temperature curve departs from eq. [12]) shifts to larger radii. This suggests that ϖ_{dep} is controlled by the disk optical depth. Indeed, we found that ϖ_{dep} correlates very well with the vertical electron scattering optical depth

$$\tau_e(\varpi_{\text{dep}}) = \int_{-\infty}^{\infty} \sigma_T \frac{\gamma}{\mu m_H} \rho(\varpi_{\text{dep}}, z) dz, \quad (13)$$

where σ_T is the electron scattering cross section, γ is the number of electrons per ion, μ is the mean molecular weight, and m_H the mass of the hydrogen atom. The values of $\tau_e(\varpi_{\text{dep}})$ for each model are listed in Table 2. We conclude that the temperature stops falling because the disk becomes (vertically) optically thin. Once the disk becomes optically thin, ionizing photons from high stellar latitudes begin to penetrate the disk, heating it back up to the optically thin radiative equilibrium temperature at large radii. Beyond this location the disk becomes roughly isothermal, behaving much like a optically thin stellar wind.

The behavior of the midplane temperature can be summarized as follows: close to the star, the temperature is described by a flat blackbody reprocessing disk, eq. (12), with

$T_\star \approx T_{\text{eff}}$ for low ρ_0 and $T_\star > T_{\text{eff}}$ for larger ρ_0 . When the vertical electron optical depth drops below $\tau_e \approx 0.075$, the temperature curve departs from eq. (12) and quickly returns to the optically thin radiative equilibrium temperature (about 60% T_{eff}) for $\varpi \gtrsim 10\text{--}30R_\star$.

We end this section with a comparison between our results and those of Millar & Marlborough (1999a,b). For the optically thin parts of the disk, our results agree — we also find a nearly constant temperature of about 60% T_{eff} . For the midplane, however, our results differ. Their temperature in the outer parts of the disk is in general lower than ours, while in the inner parts, their results are often higher. In addition, their mid-plane temperature profiles initially drop much more quickly than ours, and they sometimes have a local maximum at intermediate radii that is not seen in our results. Nonetheless, we do agree qualitatively that there is temperature minimum at small radii in the disk mid-plane.

5.3. Disk Flaring

Let us now investigate the effects of the disk flaring parameter β on the temperature structure. Experience with the flared disks of YSOs shows that the flaring controls the amount of heating versus radius, which determines the temperature versus radius (e.g., Kenyon & Hartmann 1987). In general, one finds that the smaller the flaring, the steeper the temperature gradient.

We do not, however, observe this in our results. Figure 8 shows the temperature as a function of radius for models 05, 06, 07, 08, 09 and 02, which have β ranging from 1.0 (wedge-shaped disk) to 1.5 (radially isothermal disk). The left side shows the results for three different latitudes. We see that the mid-plane temperature is very similar for all the models, but for the other latitudes, the temperatures are quite different. This difference, however, is a result of the different scaleheights probed by each latitude ray. If instead, we plot the temperatures at fixed fractions of the scaleheight above the mid-plane (right side), the curves are all very similar. We conclude that the disk flaring does not influence the disk heating versus radius.

There are probably two reasons for this: 1) at small radii, the disk surface is much less obliquely illuminated, and the direction perpendicular to the disk surface is insensitive to β (this is why the ALS model works well for this region); and 2) the outer parts of the disk are optically thin, so they heat up to the optically thin radiative equilibrium temperature, regardless of the disk flaring.

5.4. IR excess

The spectral energy distribution for Model 02 in the 0.08–1000 μm wavelength range is shown in Figure 9. Interestingly, in addition to the usual IR excess, there is a small UV excess (in the Balmer continuum) for pole-on viewing angles. Just longward of the Lyman jump, this UV excess is a result of electron scattering in the disk, which redirects some of the stellar flux into the polar direction. As the wavelength increases, bound-free emission begins to dominate, so the pole-on excess increases until the Balmer jump occurs. Beyond the Balmer jump, the f-f emission (and opacity) becomes increasingly important. As the envelope becomes optically thick, the disk develops a pseudo-photosphere that grows in size with increasing wavelength, producing the large IR excess. Since the disk is geometrically thin, the area of the pseudo-photosphere is smaller viewed edge-on than pole-on. As a result, the edge-on IR flux is about 10–50% of the pole-on flux, depending on wavelength. Note that the slope of the IR excess also depends on inclination angle.

As mentioned in the introduction, the slope of the IR excess has been used by Waters (1986) to observationally measure the radial density exponent for the circumstellar envelopes of Be stars. However, as demonstrated in section 5.2 (also see Millar & Marlborough 1998), the temperature varies throughout the disk by more than a factor of two, which raises questions about the validity and accuracy of Waters’ results.

To isolate and assess the effects of the temperature structure, we compare the IR excess,

$$Z_\lambda - 1 \equiv (F_\lambda - F_\lambda^*)/F_\lambda^*, \quad (14)$$

of the radiative equilibrium model to that of an equivalent isothermal model (i.e., one with the same density and velocity). For model 02, the best-fitting isothermal equivalent has a kinetic temperature of 11200K (about 60% of T_{eff}), and its comparison to the radiative equilibrium model is shown in Figure 10. The middle panel, which shows the ratio between the radiative equilibrium and isothermal IR excesses, indicates how well the isothermal model reproduces the full radiative equilibrium solution. Surprisingly, there is little deviation ($< 20\%$) for all inclination angles. In detail, the excesses are nearly identical for both short and long wavelengths, while the largest differences occur for intermediate wavelengths, $1 \lesssim \lambda \lesssim 100 \mu\text{m}$.

The reason an isothermal model works so well at very long wavelengths ($\lambda \gtrsim 100 \mu\text{m}$) is because the disk is so optically thick that its pseudo-photosphere occurs in the isothermal region. For the pole-on case, the effective radius, R_{eff} , of the pseudo-photosphere is the location where the vertical optical depth $\tau_\lambda(R_{\text{eff}}) = 1$. It is straightforward to show (see Appendix A, eq. [A15]) that

$$R_{\text{eff}}(\lambda) \propto \lambda^{\frac{u+2}{2n-\beta-3s/2}}, \quad (15)$$

where s and u are the exponents of the power-laws describing the temperature and Gaunt factors, respectively (see eqs. [A1] and [A2]). Using $\beta = 1.5$, $n = 3.5$, $s = 0$, and $u = 0.23$, we find (for model 02) that

$$R_{\text{eff}}(\lambda) = 1.27 R_{\star} (\lambda/1\mu\text{m})^{0.41}. \quad (16)$$

For $\lambda = 1000 \mu\text{m}$, this gives $R_{\text{eff}} \approx 21 R_{\star}$, verifying that the effective photospheric radius is indeed in the isothermal region for large wavelengths.

At shorter wavelengths ($\lambda \lesssim 100 \mu\text{m}$), the effective radius is in the non-isothermal region. As a result, the isothermal IR excess begins to differ from the radiative equilibrium excess. These differences directly reflect the temperature structure of the disk midplane. Using eq. (16) to translate from R_{eff} to wavelength, we plot (in the bottom panel of Fig. 10) the midplane temperature $T(R_{\text{eff}})$ as a function of wavelength. Note the similarity between the flux departures (middle panel) and the midplane temperatures (bottom panel). In particular, the largest difference occurs near the temperature minimum of the disk. This suggests the interesting, albeit technically challenging, possibility of inverting the observed IR excess to obtain the midplane temperature profile. The flux excess in the optically thick limit (c.f., eq. [A17]), is given approximately by

$$\begin{aligned} Z_{\lambda} - 1 &\approx \pi B_{\lambda}(R_{\text{eff}}) R_{\text{eff}}^2 / F_{\lambda}^{\star}, \\ &\approx \frac{T(R_{\text{eff}})}{T_{\text{eff}}} \left(\frac{R_{\text{eff}}}{R_{\star}} \right)^2. \end{aligned} \quad (17)$$

Consequently, the excess ratio

$$\frac{(Z_{\lambda} - 1)^{\text{MC}}}{(Z_{\lambda} - 1)^{\text{iso}}} \sim \frac{T(R_{\text{eff}}^{\text{MC}})}{T_{\text{iso}}} \left(\frac{R_{\text{eff}}^{\text{MC}}}{R_{\text{eff}}^{\text{iso}}} \right)^2, \quad (18)$$

which demonstrates why the flux departures track the the midplane temperatures. Although it appears that the flux departure depends linearly on the midplane temperature, one must recall that R_{eff} is temperature-dependent via the opacity. As the midplane radiative equilibrium temperature decreases, the opacity increases (see eq. [A5]), making $R_{\text{eff}}^{\text{MC}}$ larger than the corresponding isothermal value. This increase in the effective area of the disk pseudo-photosphere partially offsets the decrease of disk source function, $B_{\lambda}(R_{\text{eff}})$. The net result is that the flux departure is smaller than naively expected. Thus detailed modeling will be required to invert the flux departures to obtain the disk midplane temperature versus radius.

The above discussion explains the flux differences in the 1–100 μm range. It does not, however, explain why the isothermal and radiative equilibrium models agree for wavelengths $\lambda \lesssim 1 \mu\text{m}$, where the midplane temperature continues to rise well above the isothermal model

(see bottom panel of Fig. 10). To help understand this result, we show the wavelength-behavior of the IR excess versus temperature in Figure 11. As discussed previously, the IR excess increases with temperature for optically thick wavelengths. However for optically thin wavelengths, the excess decreases owing to the smaller f-f emissivity at lower temperatures (see eq. [A13]). As a consequence, marginally thick wavelengths have little temperature dependence, as shown by the $1\ \mu\text{m}$ curve (dotted line) in Figure 11. Since $(Z_\lambda - 1)$ is a weak function of T in the $0.5\text{--}1\ \mu\text{m}$ range, isothermal models reproduce the flux excess quite well in this region.

In general, we have seen that radiative equilibrium models are well-approximated by an equivalent isothermal model with a temperature $T_{\text{iso}} = 0.6T_{\text{eff}}$. However, the temperature structure is not the only factor influencing the IR SED. As shown in the appendix, the slope of the excess depends on the disk flaring parameter β (see eq. [A17]). Furthermore, as may be seen in Figures 9 and 10, the slope of the IR excess changes with inclination angle (and wavelength). The reason for the inclination-dependence is that, as R_{eff} changes with wavelength, the shape of the flared disk pseudo-photosphere is not self-similar (except for the pole-on case). In contrast for an unflared disk ($\beta = 1$), the shape is self-similar (with wavelength) for all inclination angles, so the slope of the IR excess is independent of inclination, as demonstrated in Figure 12. We conclude that the primary limitation of Waters’ method for determining the disk density distribution from the slope of the IR excess is not the isothermal assumption; it is the assumption of a particular geometry (e.g., a constant opening angle) for the disk.

6. Discussion and Conclusion

In this paper, we present a new 3-D NTLE Monte Carlo code that fully solves the radiation transfer and radiative equilibrium for arbitrary gas density and velocity distributions. Even though our method was developed independently, it is similar in many respects to the Monte Carlo transition probability method of Lucy (2002, 2003). However, our method differs from Lucy’s in a fundamental way, which is that our photon absorption and reemission mechanisms are uncorrelated — we sample the entire emissivity distribution regardless of the absorption process. This allows us to dispense with Lucy’s macro atoms, along with their associated internal transitions and Monte Carlo transition probabilities. Tests of our code against an independent (1-D spherically symmetric) NLTE code show that our method rapidly converges to the correct results, typically requiring only a few iterations. This rapid convergence also occurs for the non-trivial 2-D disk geometry investigated here.

Since the primary purpose of our NTLE Monte Carlo method is the study of gaseous

circumstellar disks, we performed an initial investigation of the temperature and ionization structure of Be star disks. Our results for the disk temperature show that its behavior is a hybrid between that of optically thick disks of Young Stellar Objects and optically thin winds from Hot Stars. We find that the temperature initially drops very quickly close to the stellar photosphere, and the temperature profile is well-described by a flat blackbody reprocessing disk (Adams et al. 1987). When the disk becomes optically thin vertically, the temperature departs from this curve and rises back to the optically thin radiative equilibrium temperature, which is approximately constant in the winds of Hot Stars. We find that the average temperature in these isothermal regions is about 60% of T_{eff} , which is cooler than the 80% value frequently quoted in the literature (e.g., Waters 1986). Similarly, the upper layers of the disk heat up to the optically thin radiative equilibrium temperature, which again is approximately isothermal. This behavior is analogous to the hot upper layers of YSO disks (see Chiang & Goldreich 1997). However, unlike YSO disks whose flaring controls their heating, we find that the disk temperature of Be star disks is influenced very little by the disk flaring.

As to be expected, we find that the disk is entirely ionized, but there is a region close to the midplane (from about 3–6 R_{\star} outwards) for which the neutral hydrogen fraction ranges from a few % up to 50%, depending on the model density. This site of low ionization coincides with the temperature minimum in the disk midplane. Because the location of the temperature minimum is controlled by the vertical optical depth, we find that as the density increases, the temperature minimum occurs at larger radii, and the disk becomes more neutral owing to the decrease in photoionization at high optical depths. This suggests the temperature minimum also is likely to be the site for the formation of low ionization state lines (such as Fe II) that produce the shell features observed in Be stars.

Finally, to investigate the consequences of the non-isothermal temperature structure on the IR excess of Be stars, we calculated the SEDs for our models and compared them to equivalent isothermal models. We find the effects of the temperature structure are small (< 20% change in the flux), and that the IR excess is well-described by an isothermal model whose temperature is about $0.6T_{\text{eff}}$. Hence the slope of the IR excess is less sensitive to the disk temperature structure than it is to the disk geometry (e.g., inclination angle and flaring). We conclude the main limitation for using the IR excess to determine disk properties is the use of an assumed disk geometry.

In the next paper of this series, we will address the question of disk geometry by self-consistently determining both the disk temperature and density. To do so, we will use the radiative equilibrium temperatures to solve the vertical hydrostatic equilibrium structure for a Keplerian disk with steady-state viscous accretion (or decretion). This self-consistent

solution for the disk structure and radiative transfer will permit us to quantitatively test whether or not the SEDs and intrinsic polarization of Be stars can be produced by a viscous decretion disk.

The authors are grateful to the referee, Dr. L.B. Lucy, for his useful comments. The authors acknowledge support from NSF grants AST-9819928 and AST-0307686. A.C.C. acknowledges partial support from Fapesp 04/07707-3.

A. IR Excess of Pole-on Flared Disks

Following a method similar to that employed by Waters (1986), we consider a star surrounded by a fully ionized disk with density given by eqs. (9) and (10). Let us assume a power-law distribution for the temperature

$$T(\bar{\varpi}) = T_0 \bar{\varpi}^{-s}, \quad (\text{A1})$$

where $\bar{\varpi} = \varpi/R_*$, as well as a power-law for the free-free plus bound-free Gaunt factors

$$g_\lambda = g_0 \left(\frac{\lambda}{\lambda_0} \right)^u. \quad (\text{A2})$$

Since we assume the disk is viewed pole-on, the intensity for $\bar{\varpi} \leq 1$ is not changed by the presence of the disk. Hence, the intensity I_λ may be written as

$$I_\lambda(\bar{\varpi}) = \begin{cases} B_\lambda^*(T_{\text{eff}}) & (\bar{\varpi} \leq 1), \\ B_\lambda^d(T) [1 - e^{-\tau_\lambda(\bar{\varpi})}] & (\bar{\varpi} > 1), \end{cases} \quad (\text{A3})$$

where we assumed, for simplicity, that the disk is vertically isothermal and that the star emits a blackbody spectrum (for the spectral range of interest, $\lambda > 1 \mu\text{m}$, a hot star emits a spectrum that is similar to a blackbody).

The optical depth along the line of sight is

$$\tau_\lambda(\bar{\varpi}) = \int_{-\infty}^{\infty} \kappa_\lambda(\bar{\varpi}) dz, \quad (\text{A4})$$

where the opacity

$$\kappa_\lambda = 3.69 \cdot 10^8 T^{-1/2} c^{-3} \lambda^3 (1 - e^{-hc/\lambda kT}) g_\lambda \frac{\gamma^2 \rho^2}{\mu^2 m_{\text{H}}^2}. \quad (\text{A5})$$

For long wavelengths and the typical temperature range of Be star disks (several thousand K), the opacity can be written as

$$\kappa_\lambda = \kappa_0 \bar{\omega}^{3s/2-2n} e^{-z^2/H^2} \lambda^{2+u}, \quad (\text{A6})$$

with

$$\kappa_0 = 1.77 \cdot 10^{-2} T_0^{-3/2} c^{-3} g_0 \lambda_0^{-u} \frac{\gamma^2 \rho_0^2}{\mu^2 m_{\text{H}}^2}. \quad (\text{A7})$$

Performing the integration in eq. (A4), we find

$$\tau_\lambda(\bar{\omega}) = \tau'_\lambda \bar{\omega}^{3s/2-2n+\beta}, \quad (\text{A8})$$

with $\tau'_\lambda \equiv \sqrt{\pi} \kappa_0 H_0 \lambda^{2+u}$.

The total flux (star plus disk) is given by

$$F_\lambda = \int_0^{2\pi} d\phi \int_0^{\bar{R}_d} I_\lambda(\bar{\omega}) \bar{\omega} d\bar{\omega}. \quad (\text{A9})$$

Defining the *excess flux* $Z_\lambda - 1 \equiv (F_\lambda - F_\lambda^*)/F_\lambda^*$, we have

$$Z_\lambda - 1 = 2 \int_1^{\bar{R}_d} \frac{B_\lambda^d}{B_\lambda^*} \left(1 - e^{-\tau'_\lambda \bar{\omega}^{3s/2-2n+\beta}}\right) \bar{\omega} d\bar{\omega}, \quad (\text{A10})$$

which can be written in the Rayleigh-Jeans limit as

$$Z_\lambda - 1 = 2 \frac{T_0}{T_{\text{eff}}} \int_1^{\bar{R}_d} \bar{\omega}^{1-s} \left(1 - e^{-\tau'_\lambda \bar{\omega}^{3s/2+\beta-2n}}\right) d\bar{\omega}. \quad (\text{A11})$$

Equation (A11) can be integrated numerically to obtain the flux excess. However in the limiting cases of optically thin and optically thick disks, useful analytical approximations can be obtained. In the optically thin case, $1 - \exp(-\tau'_\lambda \bar{\omega}^{3s/2-2n+\beta}) \approx \tau'_\lambda \bar{\omega}^{3s/2-2n+\beta}$, so eq. (A11) becomes

$$Z_\lambda - 1 = 2 \frac{T_0}{T_{\text{eff}}} \frac{\bar{R}_d^{2+s/2+\beta-2n} - 1}{2 + s/2 + \beta - 2n} \tau'_\lambda. \quad (\text{A12})$$

Because $\tau'_\lambda \propto T_0^{-3/2}$, it follows that the IR excess in the optically thin case will scale with T_0 as

$$Z_\lambda - 1 \propto T_0^{-1/2}. \quad (\text{A13})$$

In the optically thick limit, a useful approximation is to consider that most of the radiation comes from a pseudo-photosphere for which the effective radius $\bar{R}_{\text{eff}}(\lambda)$ is defined so that

$$\tau_\lambda(\bar{R}_{\text{eff}}) \equiv 1. \quad (\text{A14})$$

Using eq. (A8), we determine that

$$\bar{R}_{\text{eff}}(\lambda) = \bar{R}_0 \left(\frac{\lambda}{c} \right)^{\frac{u+2}{2n-\beta-3s/2}}, \quad (\text{A15})$$

where

$$\bar{R}_0 = \frac{(\sqrt{\pi}\kappa_0 H_0)^{(2n-\beta-3s/2)^{-1}}}{R_\star}. \quad (\text{A16})$$

With \bar{R}_{eff} so defined, the flux excess for the optically thick disk is

$$\begin{aligned} Z_\lambda - 1 &= 2 \frac{T_0}{T_{\text{eff}}} \int_1^{\bar{R}_{\text{eff}}} \bar{\omega}^{1-s} d\bar{\omega}, \\ &= \frac{2}{2-s} \frac{T_0}{T_{\text{eff}}} \left[\bar{R}_0^{2-s} \left(\frac{\lambda}{c} \right)^{\frac{(u+2)(2-s)}{2n-\beta-3s/2}} - 1 \right]. \end{aligned} \quad (\text{A17})$$

REFERENCES

- Adams, F. C., Lada, C. J., & Shu, F. H. 1987, *ApJ*, 312, 788 (ALS)
- Bjorkman, J. E. 1997, *Circumstellar Disks*, in *Stellar Atmospheres: Theory and Observations*, ed. J. P. de Greve, R. Blomme, & H. Hensberge (New York: Springer)
- Bjorkman, J. E. & Wood, K. 2001, *ApJ*, 554, 615
- Cayrel, R. 1963, *C. R. Acad. Sci. Paris*, 257, 3309
- Cassinelli, J. P., & Hartmann, L. 1977, *ApJ*, 212, 488
- Coté, J., & Waters, L. B. F. M. 1987, *A&A*, 176, 93
- Chiang, E. I., & Goldreich, P. 1997, *ApJ*, 490, 368
- D’Alessio, P., Canto, J., Calvet, N., & Lizano, S. 1998, *ApJ*, 500, 411
- Drew, J. E. 1989, *ApJS*, 71, 267
- Dullemond, C. P. 2002, *A&A*, 395, 853
- Gehrz, R.D., Hackwell, J.A., & Jones, T.W. 1974, *ApJ*, 191, 675
- Hanuschik, R. W. 1988, *A&A*, 190, 187
- Hanuschik, R. W. 1995, *A&A*, 295, 423

- Hanuschik, R. W. 1996, *A&A*, 308, 170
- Hanuschik, R. W. 2000, *ASP Conf. Ser. 214: IAU Colloq. 175: The Be Phenomenon in Early-Type Stars*, 214, 518
- Hartmann, L. 1998, *Accretion Processes in Star Formation* (Cambridge: Cambridge Univ. Press)
- Hummel, W., & Vrancken, M. 2000, *A&A*, 359, 1075
- Jones, C. E., Sigut, T. A. A., & Marlborough, J. M. 2004, *MNRAS*, 352, 841
- Kenyon, S. J., & Hartmann, L. 1987, *ApJ*, 323, 714
- Klein, R. I., & Castor, J. I. 1978, *ApJ*, 220, 902
- Kurucz, R. L. 1979, *ApJS*, 40, 1
- Kurucz, R. L. 1994, *Kurucz CD ROM 19, Solar Model Abundance Model Atmospheres*, (Cambridge: Smithsonian Astrophysical Observatory)
- Lamers, H. J. G. L. M., & Waters, L. B. F. M. 1984, *A&A*, 136, 37
- Lee, U., Osaki, Y., & Saio, H. 1991, *MNRAS*, 250, 432
- Lucy, L.B. 1999, *A&A*, 344, 282 (L99)
- Lucy, L.B. 2002, *A&A*, 384, 725 (L02)
- Lucy, L.B. 2003, *A&A*, 403, 261 (L03)
- Lucy, L.B. 2005, *A&A*, 429, 31 (L05)
- Lynden-Bell, D., & Pringle, J. E. 1974, *MNRAS*, 168, 603
- MacFarlane, J. J., Waldron, W. L., Corcoran, M. F., Wolff, M. J., Wang, P., & Cassinelli, J. P. 1993, *ApJ*, 419, 813
- Maheswaran, M. 2003, *ApJ*, 592, 1156
- Millar, C. E., & Marlborough, J. M. 1998, *ApJ*, 494, 715
- Millar, C. E., & Marlborough, J. M. 1999a, *ApJ*, 516, 276
- Millar, C. E., & Marlborough, J. M. 1999b, *ApJ*, 526, 400

- Narita, S., Kiguchi, M., & Hayashi, C. 1994, PASJ, 46, 575
- Okazaki, A. T. 1991, PASJ, 43, 75
- Poeckert, R., & Marlborough, J. M. 1978, ApJ, 220, 940
- Porter, J. M. 1999, A&A, 348, 512
- Porter, J. M., & Rivinius, Th. 2003, PASP, 115, 1153
- Quirrenbach, A., Bjorkman, K. S., Bjorkman, J. E., Hummel, C. A., Buscher, D. F., Armstrong, J. T., Mozurkewich, D., Elias, N. M., II, & Babler, B. L. 1997, ApJ, 479, 477
- Walker, C., Wood, K., Lada, C. J., Robitaille, T., Bjorkman, J. E., & Whitney, B. A. 2004, MNRAS, 351, 607
- Waters, L. B. F. M. 1986, A&A, 162, 121
- Waters, L. B. F. M., Coté, J., & Lamers, H. J. G. L. M. 1987, A&A, 185, 206
- Whitney, B. A., Wood, K., Bjorkman, J. E., & Wolff, M. J. 2003, ApJ, 591, 1049
- Wood, K., Bjorkman, K. S., & Bjorkman, J. E. 1997, ApJ, 477, 926
- Wood, K., Wolff, M. J., Bjorkman, J. E., & Whitney, B. A. 2002, ApJ, 564, 887
- Wright, A. P., & Barlow, M. J. 1975, MNRAS, 170, 41

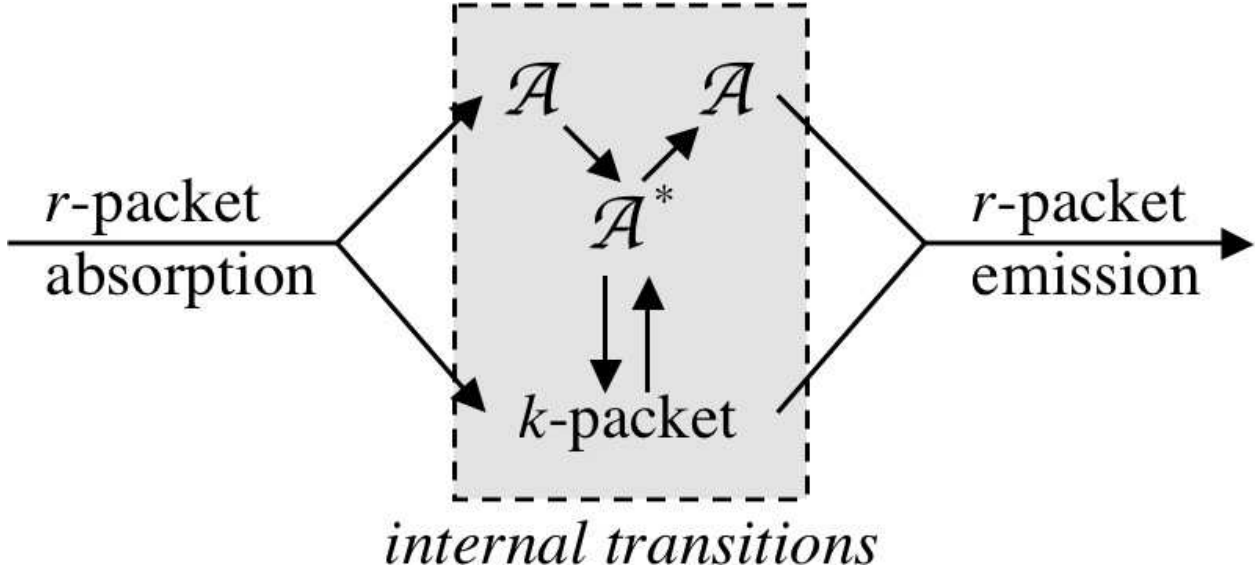


Fig. 1.— Photon-Macro Atom Interaction. In Lucy’s method (Lucy 2002) when a photon (r -packet) is absorbed, it either activates the macro atom ($A \rightarrow A^*$), or it is converted into a k -packet (free electron energy). If it activates the macro atom, the macro atom undergoes internal transitions (possibly producing a k -packet and deactivating) until a photon packet is eventually reemitted ($A^* \rightarrow A$). If a k -packet is produced, the k -packet can either reactivate the macro atom, or it can emit a photon packet directly. In any case, the absorption of a photon eventually leads to the reemission of a new photon.

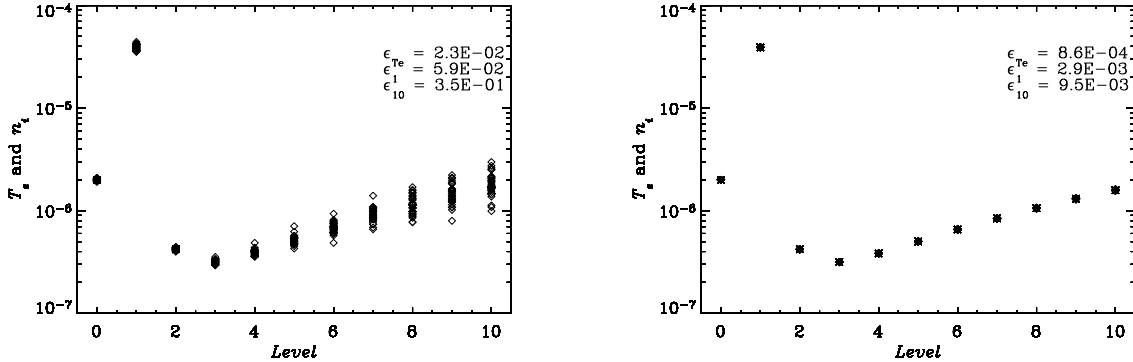


Fig. 2.— Stability Test. The electron temperature (level 0 corresponds to $T_e/10^{10}$) and hydrogen level populations (up to level 10) are shown for 30 successive iterations. The left panel shows the results (triangles) for $N = 10^4$ PPs, while the right panel is for $N = 10^7$ PPs. Note that the variation of the values is centered on the correct (LTE) values (stars). The R.M.S. variation, ϵ , for various levels is indicated.

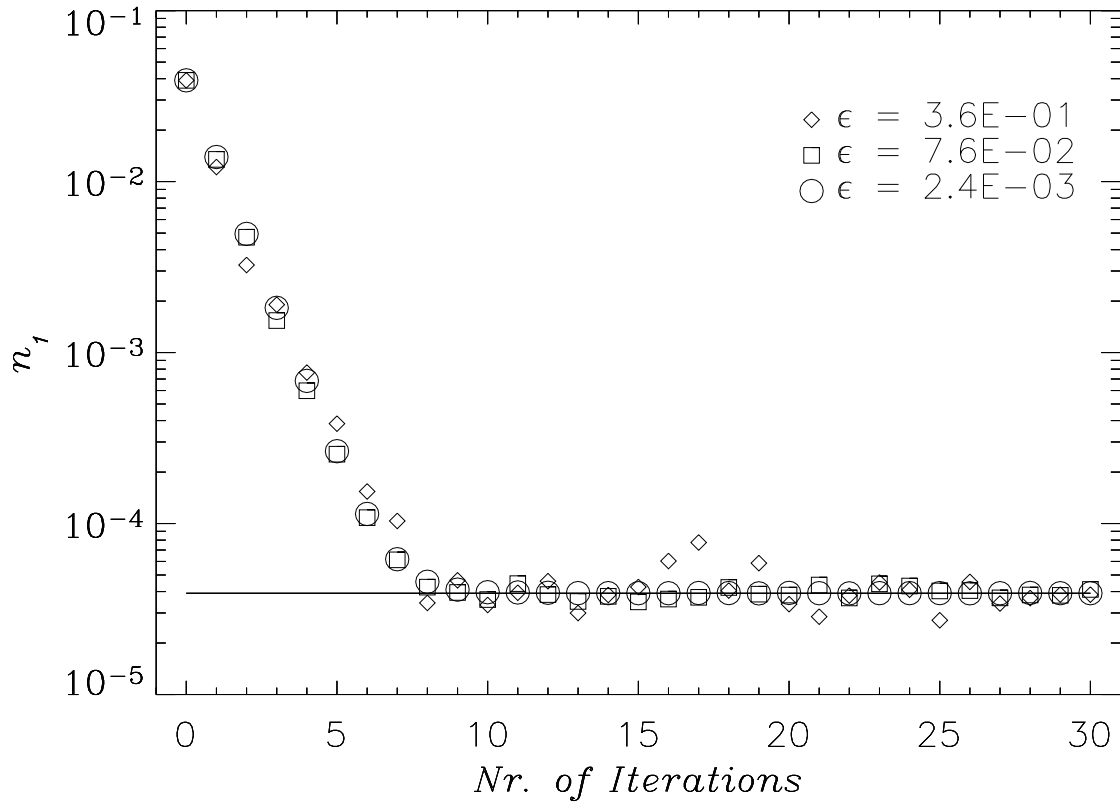


Fig. 3.— Convergence Test. The hydrogen ground level population is shown for a sequence of 30 iterations (Diamonds: $N = 10^3$; Squares: $N = 10^4$; Circles: $N = 10^7$). Iteration zero refers to the initial population. The straight line shows the correct level population.

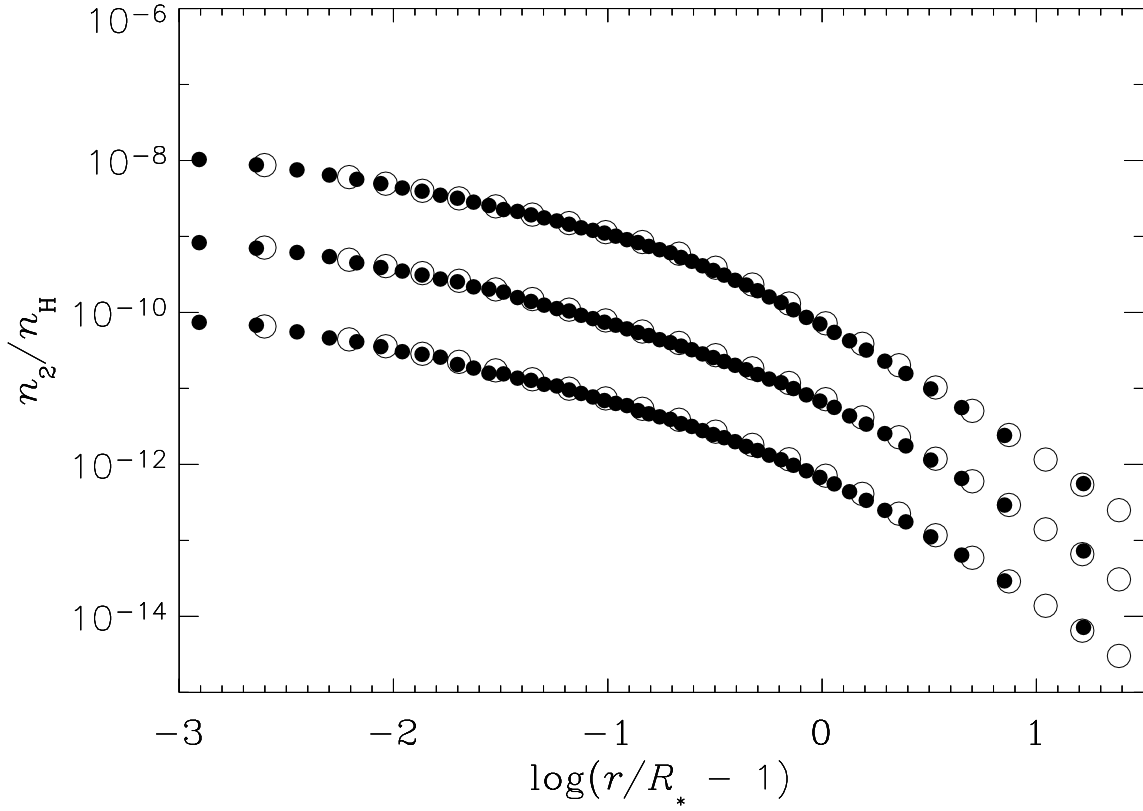


Fig. 4.— NLTE Validation. Comparison between the results of the MacFarlane et al. (1993) code (open circles) and our code (filled circles). Shown are the $n = 2$ hydrogen level populations as a function of distance from the star. From bottom to top, the curves are for $\log \dot{M} = -8.7$, -7.7 and -6.7 , respectively.

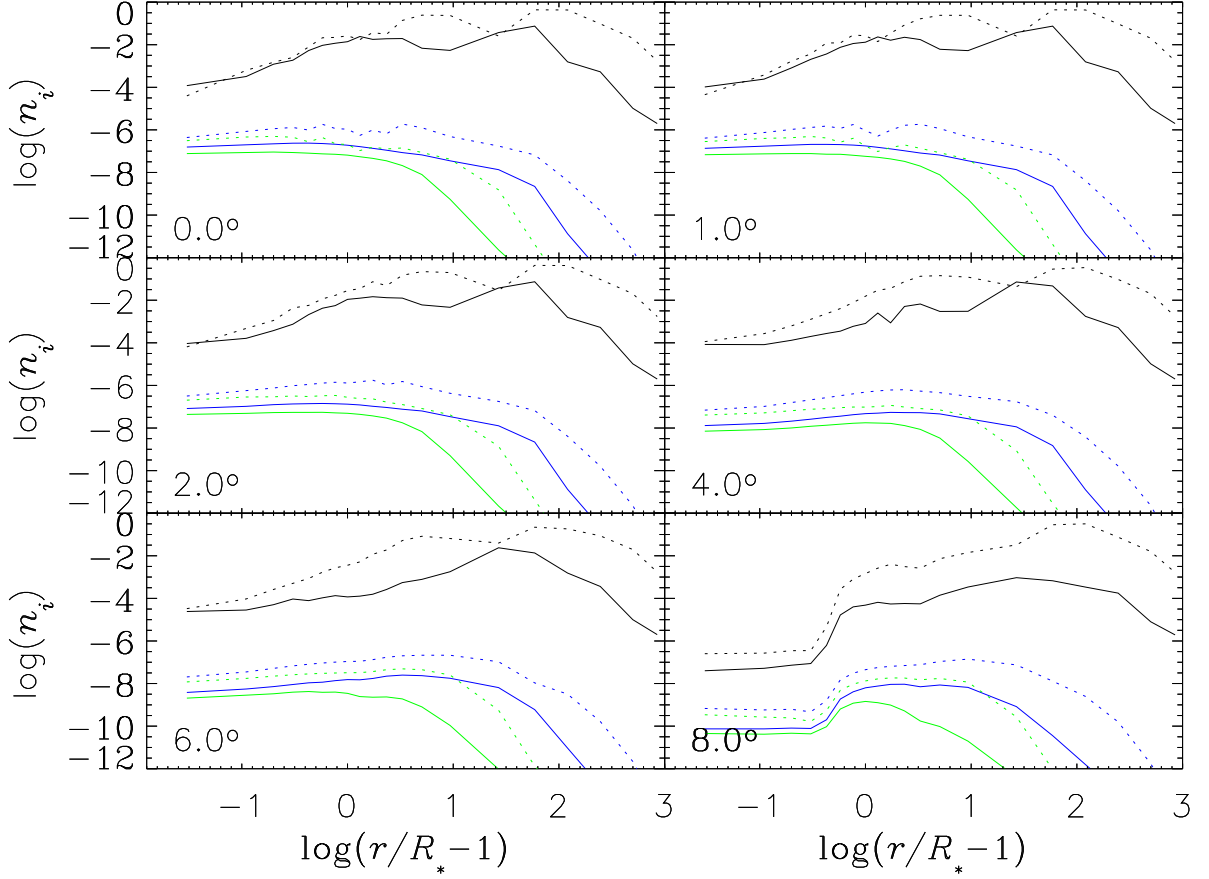


Fig. 5.— Hydrogen Level Populations. Shown are the level populations for $n = 1$ (black), $n = 2$ (blue), and $n = 3$ (green) as a function of radius. The solid curves are for model 01 (low density) while the dotted curves are for model 04 (high density). Each panel shows the populations at a given latitude (angle above midplane), as indicated.

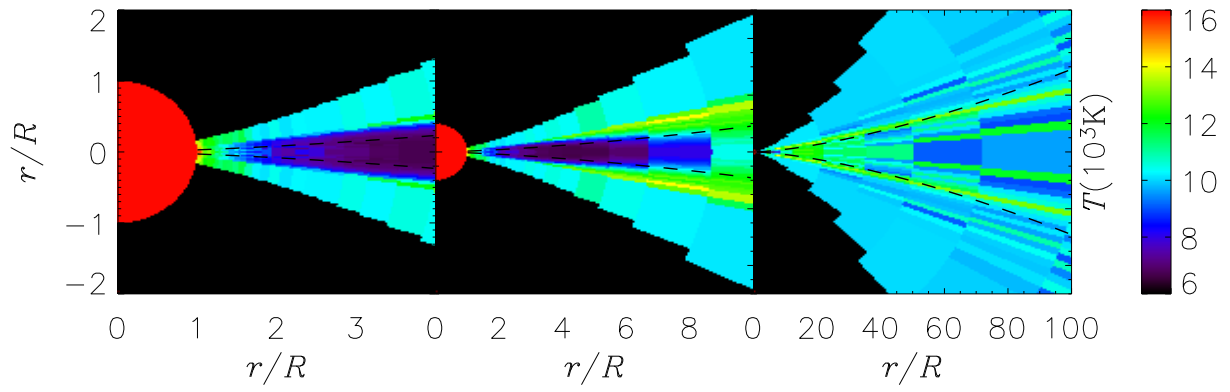


Fig. 6.— Disk Temperature. Shown is the temperature structure for model 02 at three radial scales. The dashed lines correspond to the curves $|z| = H(\varpi)$.

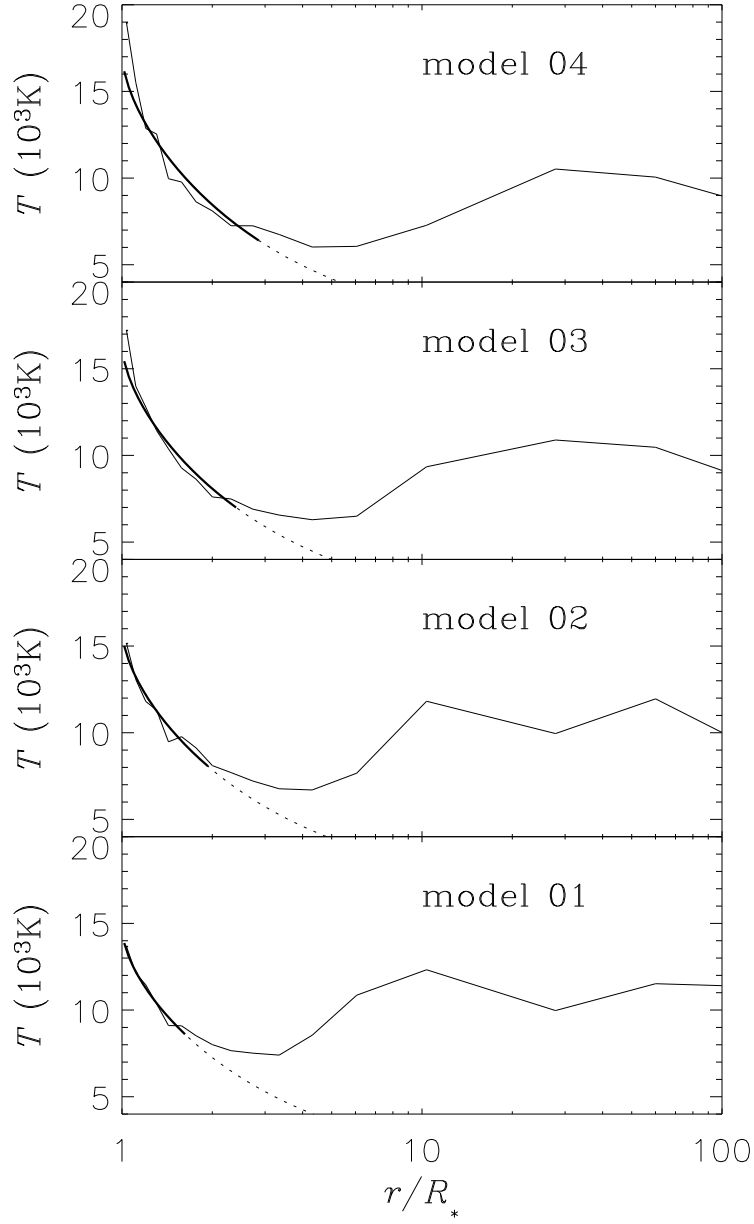


Fig. 7.— Mid-plane Temperature. The radial dependence of the equatorial temperature is shown for models 01, 02, 03, and 04 (increasing density, respectively). The thick curve is a fit, for ϖ between R_* and ϖ_{dep} , to a flat blackbody reprocessing disk (Adams et al. 1987).

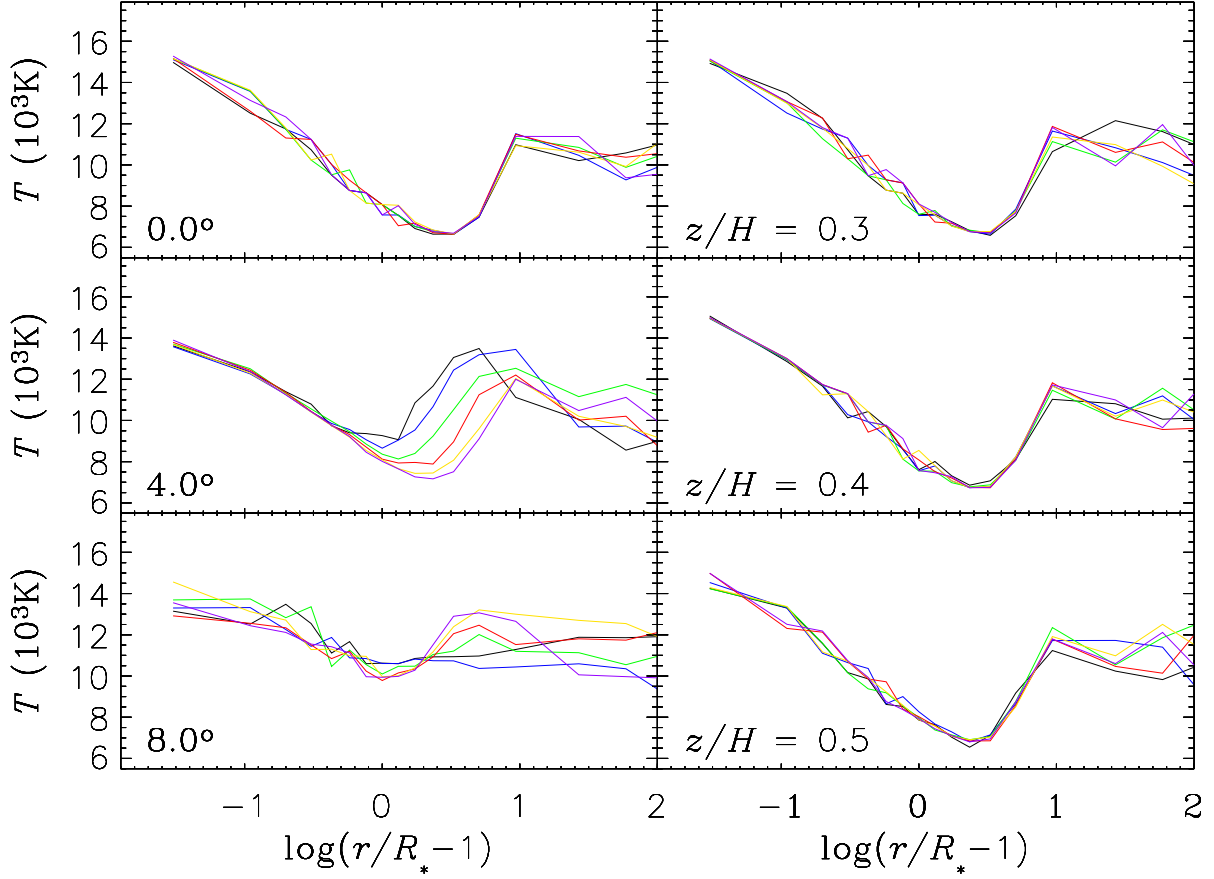


Fig. 8.— Effects of Disk Flaring. The temperature versus radius is shown for six values of the disk flaring exponent, $\beta = 1.0$ – 1.5 in steps of 0.1 (black, blue, green, red, orange, and purple lines, respectively). The different panels show the temperature along rays with a given latitude (left) and for a given fraction of the disk scale height (right).

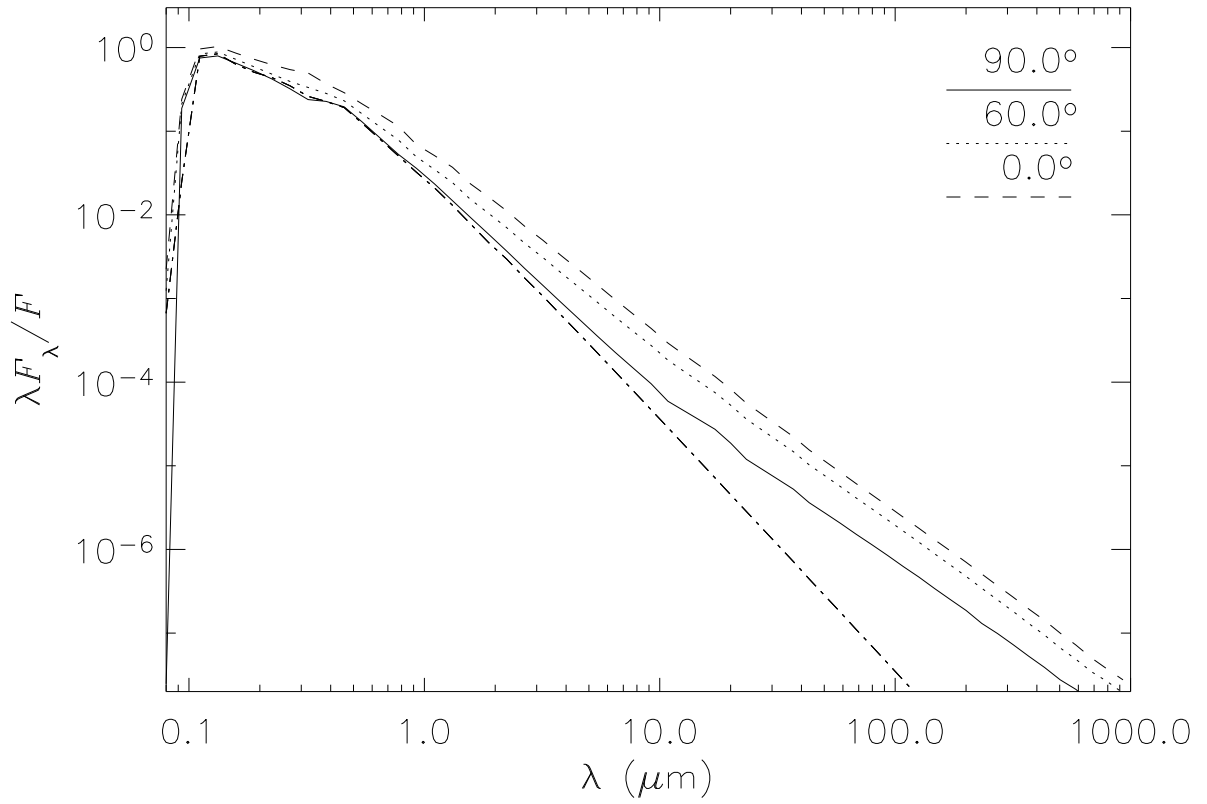


Fig. 9.— Spectral Energy Distribution. Shown is the emergent flux for Model 02, viewed at three different inclinations, as indicated. The dash-dotted line indicates the input flux from the star (a 19000 K Kurucz model atmosphere).

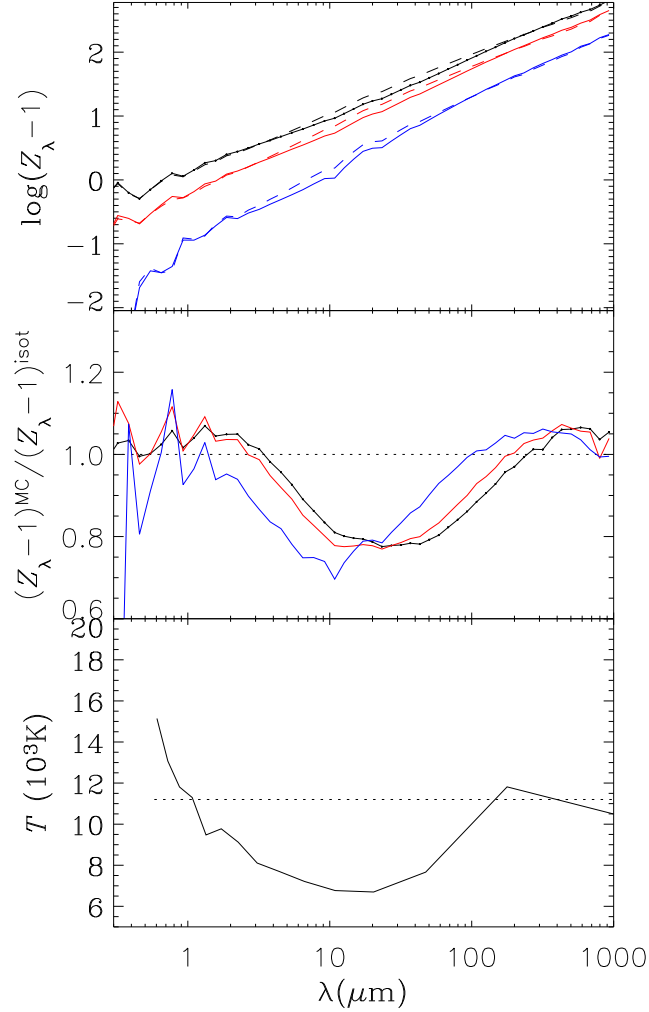


Fig. 10.— IR Excess for Model 02. The top panel compares the radiative equilibrium IR excess (solid lines) to that of an equivalent isothermal model (dashed lines) for three inclinations: pole-on (black), 60° (red), and edge-on (blue). The isothermal model has a temperature $T_{\text{iso}} = 0.6T_{\text{eff}}$, which yields the best fit. The middle panel shows the ratio of the IR excesses for the radiative equilibrium and isothermal models, while the bottom panel shows the disk mid-plane temperature at $R_{\text{eff}}(\lambda)$, the radius of the pseudo-photosphere as a function of wavelength (see text). Note that the deviation between the radiative equilibrium and isothermal excesses roughly tracks the shape of the mid-plane temperature.

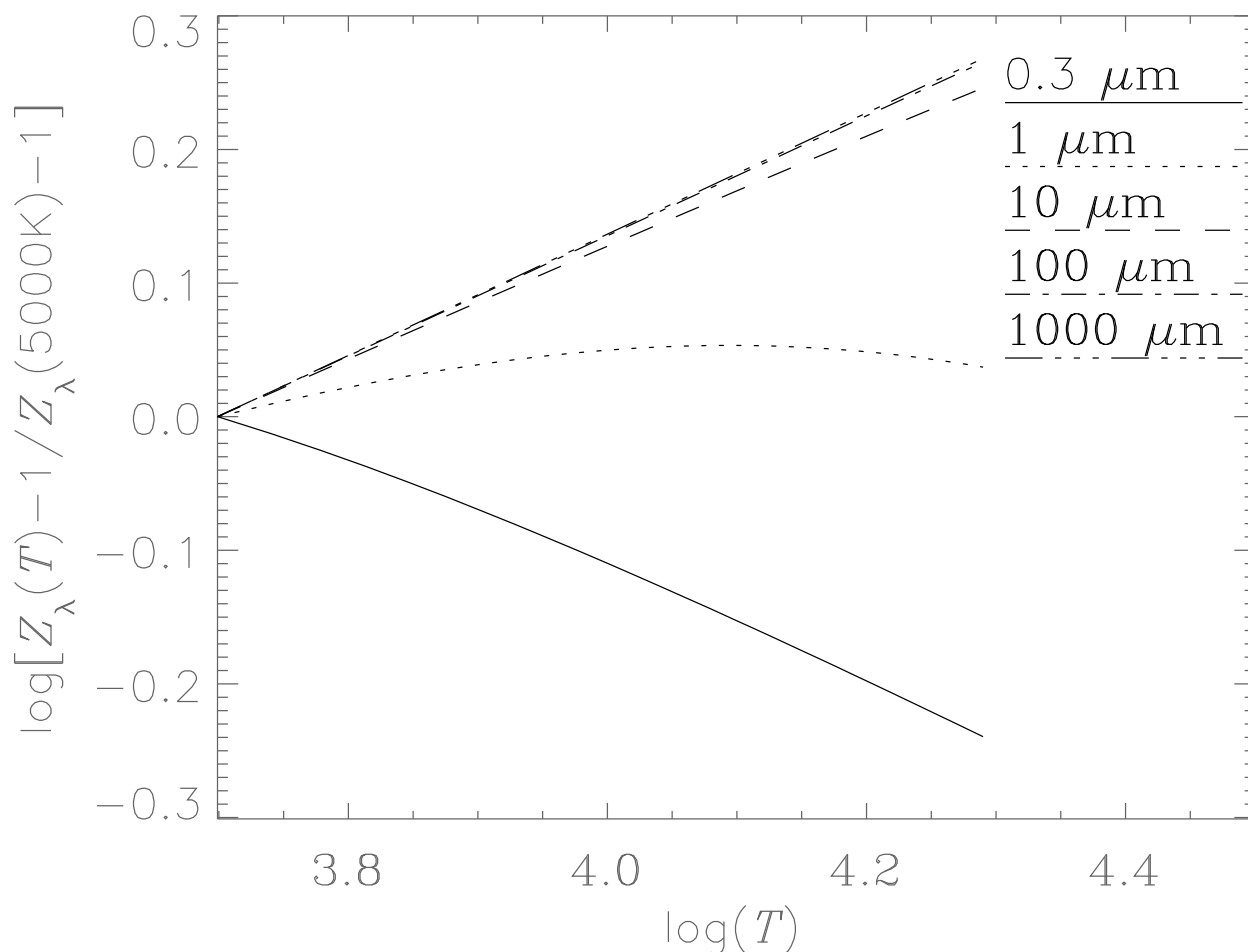


Fig. 11.— Temperature-dependence of the IR Excess. The IR excess as a function of temperature is shown for different wavelengths, as indicated. Each curve was normalized to the excess at 5000 K. Note that, for the optically thin (shorter) wavelengths, the excess decreases with increasing temperature, while for the optically thick (longer) wavelengths, the excess increases.

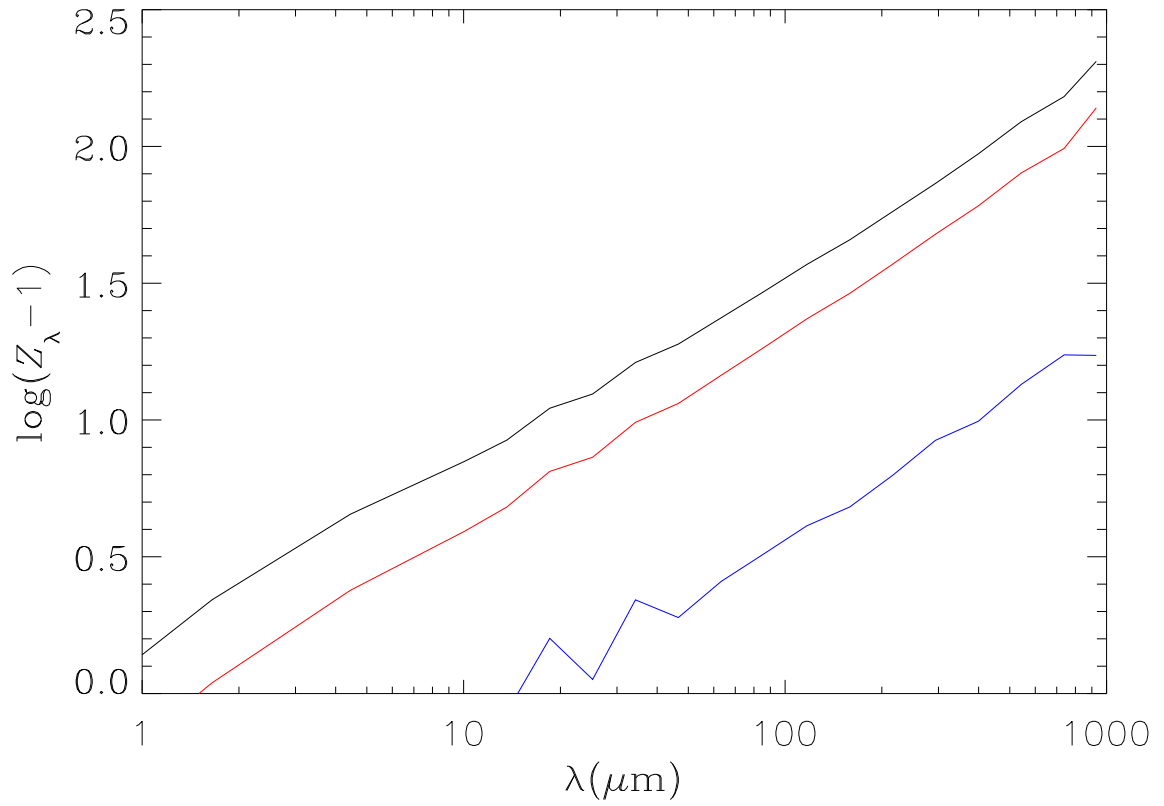


Fig. 12.— Infrared excess vs. wavelength for model 05 ($\beta = 1.0$). Shown are results for three inclinations: pole-on (black), 60° (red), and edge-on (blue).

Table 1. Adopted Stellar Parameters.

Parameter	Value
Spectral Type ...	B3 IV
R_{\star}	$5.6R_{\odot}$
T_{eff}	19000 K
$\log g$	4
M_{\star}	$9.2M_{\odot}$
v_{crit}	560 km s^{-1}

Table 2. Disk Model Parameters.

Model	ρ_0 (g cm^{-3})	β	T_{\star} (K)	ϖ_{dep} (R_{\star})	$\tau_e(\varpi_{\text{dep}})$
01	$1.66 \cdot 10^{-11}$	1.5	17600	1.7	.063
02	$4.15 \cdot 10^{-11}$	1.5	19100	2.0	.081
03	$8.39 \cdot 10^{-11}$	1.5	19600	2.5	.072
04	$1.66 \cdot 10^{-10}$	1.5	20500	3.0	.081
05	$4.15 \cdot 10^{-11}$	1.0	18600	2.0	.083
06	$4.15 \cdot 10^{-11}$	1.1	18800	2.0	.078
07	$4.15 \cdot 10^{-11}$	1.2	18200	2.0	.077
08	$4.15 \cdot 10^{-11}$	1.3	18700	2.0	.080
09	$4.15 \cdot 10^{-11}$	1.4	18600	2.0	.085